Phase-Sensitive Imaging of Ferromagnetic Resonance Using Ultrafast Heat Pulses

Feng Guo, J. M. Bartell, D. H. Ngai, and G. D. Fuchs*
Cornell University, Ithaca, New York 14853, USA
(Received 8 July 2015; revised manuscript received 9 September 2015; published 9 October 2015)

Measuring local magnetization dynamics and its spatial variation is essential for advancements in spintronics and relevant applications. Here we demonstrate a phase-sensitive imaging technique for studying patterned magnetic structures based on picosecond laser heating. With the time-resolved anomalous Nernst effect (TRANE) and extensions, we simultaneously image the dynamic magnetization and rf driving current density. The stroboscopic detection implemented in TRANE microscopy provides access to both amplitude and phase information of the ferromagnetic resonance (FMR) and rf current. Using this approach, we measure the spatial variation of the Oersted driving field angle across a uniform channel. In a spatially nonuniform sample with a cross shape, a strong spatial variation for the rf current as well as FMR precession is observed. We find that both the amplitude and the phase of local FMR precession are closely related to those of the rf current.

DOI: 10.1103/PhysRevApplied.4.044004

I. BACKGROUND

Improving the detection of local ferromagnetic resonance (FMR) expands our ability to study magnetization dynamics and the underlying physics. From the application standpoint, appropriate measurement techniques are pivotal to develop and advance the next-generation magnetic storage and memory technology. Here we present a study on local FMR measurement in conjunction with excitation current. We apply stroboscopic measurement techniques based on ultrafast heat pulses to detect both the rf current and FMR signal simultaneously. By measuring both absolute phase and amplitude, we establish the relation between the driving current and corresponding magnetic response.

Several compelling techniques have been developed to study local magnetization dynamics, including microfocused Brillouin light scattering [1–4], force-based FMR detection [5–11], time-resolved Kerr microscopy [12–15], and x-ray magnetic circular dichroism [16–18], to name a few. Very recently, time-resolved anomalous Nernst effect (TRANE) microscopy has been developed for magnetic imaging as well as for stroboscopic FMR measurement [19].

Relevant to this work, spin-torque ferromagnetic resonance (ST FMR) [20–22] is a phase-sensitive technique that has been effective for studying spin-Hall-effect physics. The rectified dc signal measured with ST FMR is sensitive to the relative phase between the magnetization precession and the rf current, while TRANE microscopy probes the absolute precession phase. Also, ST FMR lacks the ability to probe the spatial variations that might occur in the devices. In addition to the existing electrical measurements, a phase-sensitive FMR measurement technique using the magneto-optic Kerr effect has also been recently reported [23].

Here we introduce a method of phase-sensitive magnetic imaging based on TRANE microscopy, combining spatial scanning and phase-detection capabilities. We demonstrate simultaneous detection of local spin-wave resonance and rf current. This capability enables imaging of the magnetic dynamic susceptibility in the gigahertz range. A distinct feature of this work is that we demonstrate a technique for measuring the local amplitude and phase of both the magnetic precession and microwave excitation current. This feature enables us to image the spatial variations of the magnetic dynamics that are lost in other electrical measurement techniques. The relationship between excitation and response is relevant in understanding the origin of the torques that drive magnetic dynamics.

We first describe the essential measurement procedure and then explain the detection method of both the rf-driving current and the FMR response. Next, we quantitatively analyze the FMR phase in response to a varied rf current phase and show that the phase-sensitive FMR spectra measured in a uniform current channel reveal the local driving field orientation. Using phase-dependent imaging, we also demonstrate that a spatially nonuniform channel shows a strong spatial variation, both for the FMR and rf current.

II. INTRODUCTION TO TRANE MICROSCOPY

As its name suggests, the heart of TRANE microscopy is the anomalous Nernst effect (ANE) [24–28]: an electric field, $E_{\mathrm{ANE}} = -N\mu_0 \mathbf{m} \times \nabla T$ produces an ANE voltage V_{ANE} associated with the magnetization $\mathbf{m}$ through the anomalous Nernst coefficient N and the temperature gradient ∇T. We use a hybrid measurement scheme that combines optical generation of a pulsed thermal gradient and electrical detection of an ANE voltage, in order to

*gdf9@cornell.edu

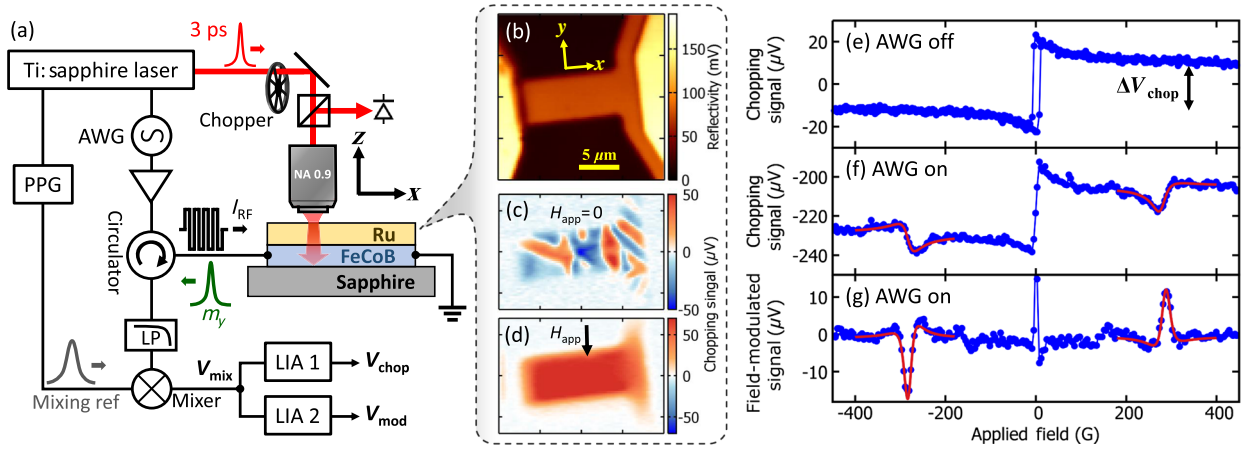

FIG. 1. (a) Schematics of the TRANE setup. (b) Reflected laser intensity shows a micrograph of the sample. Without any applied current, the chopping referenced signal measures the y component of the magnetization m_y in a demagnetized state at zero field (c) showing domain patterns and a saturated state (d) under a large applied field. (e) Hysteresis loop measured with the chopping signal with an in-plane applied field (5° away from the sample length direction). No current or modulation field are applied in this measurement. (f) A similar hysteresis loop measurement with a 5.7 GHz rf driving current. Ferromagnetic resonance signal is seen for both applied field directions near ±280 G. The large constant background voltage is due to the combination of local heating and the rf current. (g) The field-modulated signal sensitive only to the magnetic response is measured simultaneously with the chopping signal in (f). The red curves in (f) and (g) are the fits for ferromagnetic resonance. All the data shown in (e)–(g) are the mixed signals locked into the chopping reference (V_{chop}) and the field-modulating reference (V_{mod}).

stroboscopically detect the transient local magnetization. We point out that the spatial and temporal resolutions of the TRANE microscopy are ultimately determined by the spatial and temporal profiles of the thermal gradient. With a ∇T along the z direction and a pair of contacts along the x direction (Fig. 1), the measured ANE voltage is sensitive to the y component of the local magnetization, m_y.

Figure 1(a) depicts the schematics of the TRANE setup. A vertical thermal gradient is generated by a 792 nm Ti:sapphire laser with 3 ps long pulses and a 25.3 MHz repetition rate. The laser intensity is also modulated at 100 kHz using a polarizer and a photoelastic modulator. To create a rf driving field, we use an arbitrary waveform generator (AWG) that applies a continuous waveform rf current to the sample via a circulator. The laser and AWG are synchronized such that there is a constant phase relation between the rf current and the laser pulse train, which allows us to stroboscopically probe the instantaneous magnetization of the spin waves. Each laser pulse generates a pulsed signal, and the voltage pulse is demodulated in a mixer by combining it with a 1.5 ns duration electrical reference pulse that enters the mixer at the same time. The mixed output voltage is then measured by lock-in amplifiers. The details of the experimental configurations, including laser fluence, spatial resolution, and the simulated temporal and spatial profiles of both the thermal gradient and temperature have been discussed in our prior work [19].

In the following, we first discuss the various origins of the signal, followed by the measured spectra that contain both magnetic and rf current information. There are two signals generated by the laser pulses. Besides the above-mentioned magnetic term from the ANE voltage, an increase in the sample resistance ΔR_{heat} induced by local laser heating also contributes to the total voltage pulse generated across the sample:

$$V_{sample} = V_{ANE} + V_J. \tag{1}$$

Here, the second term $V_J = -I(t)\Delta R_{heat}(t)$ [29] is determined by the instantaneous local current following through the heated volume: $I(t) = I^0_{rf}\sin(\omega t + \varphi_{rf})$, in which I^0_{rf} is the local rf current amplitude, ω is the current frequency, and φ_{rf} is the rf current phase. As will be described later, we use V_J to measure the phase and magnitude of the local rf current. After the mixer, the voltage pulse V_{sample} from the sample is converted to a mixed signal V_{mix}. A lock-in amplifier is used to measure the signal with respect to the chopping reference, which we refer to as V_{chop}. Furthermore, to reject the nonmagnetic background, we also apply a 350 Hz, 7 G modulation field for measuring the FMR signal. The field-modulated signal $V_{mod}(H)$, which is proportional to $\partial V_{mix}(H)/\partial H$, is measured as a function of the applied field while recording the FMR spectra.

The samples consist of $Fe_{60}Co_{20}B_{20}$ (4 nm)/Ru (4 nm) bilayers deposited on the sapphire substrate as a heat sink. The bar samples have a dimension of $5\,\mu m \times 12\,\mu m$ and have a resistance of about 300 Ω. We choose this simple bilayer structure to minimize the potential spin Hall effect, as confirmed by a separate ST FMR experiment ($J_s/J_c = 0.015 \pm 0.009$, which is several times smaller than the reported values for platinum [22,30–33]). The Oersted field has a known spatial profile determined by the

current. Therefore, using the Oersted field as the only driving torque simplifies the data interpretation and helps us to establish the phase analysis.

Examples of measured spectra are shown in Figs. 1(e)–1(g). With the AWG off, the chopping signal contains only the ANE signal. Figure 1(e) shows a hysteresis loop, with an in-plane field aligned 5° off from the length of the bar (x direction). The voltage difference between magnetization saturated in opposite directions $\Delta V_{\rm chop}$ corresponds to the y component of the saturation magnetization: $2M_s \sin 5°$. However, when the AWG is turned on, a 5.7 GHz rf current creates a large background due to the contribution from V_J. This constant background is determined by the fixed phase of the rf current with respect to the laser stroboscope. As we discuss later, the voltage background in the chopping signal indeed depends on the AWG phase. Nevertheless, the signal due to magnetic reversal $\Delta V_{\rm chop}$ remains the same, as shown in Fig. 1(f). As a result of the rf excitation current, a FMR precession signal is also observed for both field directions. By the comparing the FMR signal to the $\Delta V_{\rm chop}$, we calculate the precession angle to be $(1.5 \pm 0.1)°$ [34]. Finally, to isolate the magnetic signal from the nonmagnetic rf current contribution, a field-modulated signal $V_{\rm mod}(H)$ is recorded simultaneously, as shown in Fig. 1(g). Only the FMR signal is revealed by locking into the field modulation, along with a peak near zero field due to the magnetization reversal.

III. RESULTS AND DISCUSSION

In this section, we focus on characterizing the precession phase of the measured FMR spectra. We measure the FMR precession phase $\varphi_{\rm FMR}$ through the line shape of the spectra. The field-modulated spectrum is a linear combination of the real (χ') and imaginary (χ'') dynamic susceptibilities given by [35]

$$V_{\rm mod}(H) \propto \frac{d\chi'(H)}{dH}\cos\varphi_{\rm FMR} + \frac{d\chi''(H)}{dH}\sin\varphi_{\rm FMR}. \quad (2)$$

The precession phase $\varphi_{\rm FMR}$ is directly measured from the FMR spectrum, and it depends on the phase of the rf current at the time of the stroboscopic probe, as we will discuss in the following.

To vary the rf current phase, we use the AWG to tune the relative phase of the output waveform, which we define as $\varphi_{\rm AWG}$. Nevertheless, $\varphi_{\rm rf} \neq \varphi_{\rm AWG}$, in general, since there is an initial current phase randomly determined upon AWG triggering ($\varphi^0_{\rm AWG}$). Once the AWG is triggered and synchronized with the laser pulses, $\varphi^0_{\rm AWG}$ remains constant throughout the measurements, and it can be determined as shown later. Thus, the resultant rf current phase is

$$\varphi_{\rm rf} = \varphi_{\rm AWG} - \varphi^0_{\rm AWG}. \quad (3)$$

Figure 2 shows the $\varphi_{\rm AWG}$-dependent FMR spectra measured at the center of the bar sample for both positive and negative applied fields. For a quasiuniform FMR mode,

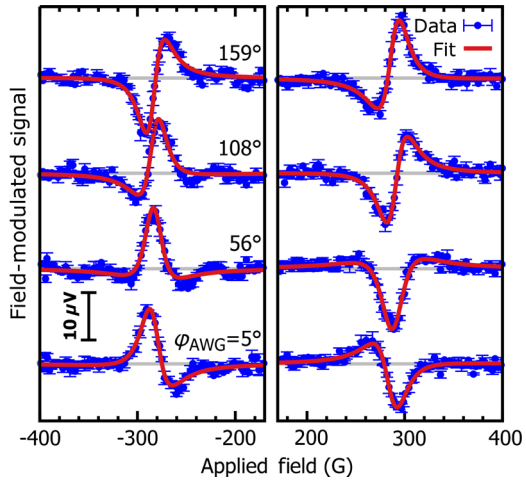

FIG. 2. Examples of field-modulated FMR spectra measured as a function of AWG phase, $\varphi_{\rm AWG}$, for both negative (left) and positive (right) field directions.

we adopt a macrospin model using the Landau-Lifshitz-Gilbert equation with an oscillating Oersted driving field. The FMR precession phases at positive ($\varphi^+_{\rm FMR}$) and negative ($\varphi^-_{\rm FMR}$) fields can be written as

$$\varphi^+_{\rm FMR} = \varphi_{\rm rf} - 90° + \theta_{\rm Oe}, \quad (4a)$$

$$\varphi^-_{\rm FMR} = -\varphi_{\rm rf} - 90° + \theta_{\rm Oe}, \quad (4b)$$

where $\theta_{\rm Oe}$ is the change in the precession phase due to an effective Oersted field angle with respect to the sample plane. The sign change under magnetic-field reversal results from the precession orientation; the term $-90°$ originates from the fact the magnetic response is 90° behind the driving field (note that at resonance $\chi'' = 0$).

At the center of the bar structure, we expect an in-plane Oersted driving field ($\theta_{\rm Oe} = 0$). After including the initial AWG phase, the intersection of Eqs. (4a) and (4b) ($\varphi^{\rm intersec}_{\rm AWG}, \varphi^{\rm intersec}_{\rm FMR}$) locates at $\varphi^{\rm intersec}_{\rm AWG} = \varphi^0_{\rm AWG}$ and $\varphi^{\rm intersec}_{\rm FMR} = -90°$. The measured FMR phase from Fig. 2 as a function of the AWG phase (also the calculated rf current phase using the measured $\varphi^0_{\rm AWG}$ [36]) is summarized in Fig. 3(a). The fitted slope for positive (negative) field is 1.01 ± 0.03 (-1.07 ± 0.02), consistent with the prediction of Eq. (4). At the point of intersection, $\varphi^{\rm intersec}_{\rm FMR} = (-87.4 \pm 4.1)°$, in agreement with the predicted value of $-90°$.

The rf current phase is also separately measured with the chopping reference signal $V_{\rm chop}$ shown in Fig. 3(b). A sinusoidal waveform is seen as expected. As a subtle point, the intersection in Fig. 3(a) does not exactly align with the zero phase in Fig. 3(b), as illustrated by the gray lines. Instead, a phase discrepancy of 20.6° between the rf current and the FMR signal is found. In the following, we explain the discrepancy by a difference in the temporal evolution of the $V_{\rm ANE}$ and V_J pulses that contribute to the signal. The phase measured with the $V_{\rm ANE}$ voltage pulse depends on

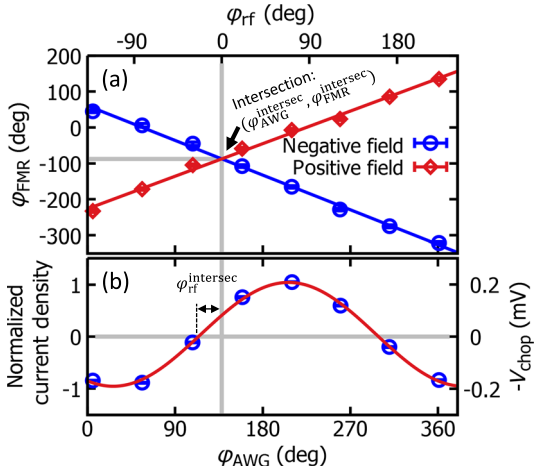

FIG. 3. (a) FMR precession phases (φ_{FMR}) of both positive (diamonds) and negative (circles) field directions as functions of an increasing AWG phase (φ_{AWG}). φ_{FMR} is measured from fitting the spectra such as those shown in Fig. 2, with the laser placed at the center of the sample. The intersection of the positive and negative field curves is located at $\varphi_{AWG}^{intersec} = (137.9 \pm 4.0)°$ and $\varphi_{FMR}^{intersec} = (-87.4 \pm 4.1)°$. (b) The normalized rf current density is measured as a function of φ_{AWG} through the chopping reference voltage. The red curve is a sinusoidal fit. The intersection in (a) corresponds to a rf current phase of $\varphi_{rf}^{intersec} = (20.6 \pm 4.2)°$, which is the difference in the current phase measured in (a) and (b).

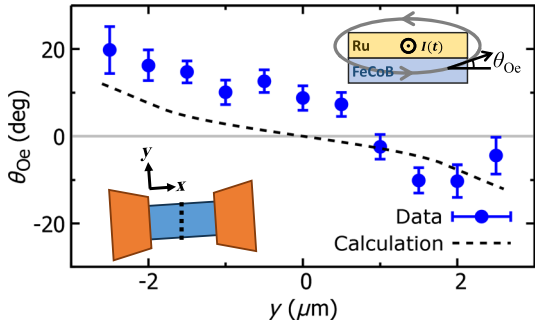

FIG. 4. The effective Oersted field angle (θ_{Oe}) measured through the FMR phases as a function of the laser's y position. The numerically computed θ_{Oe} (dashed curve) for a perfectly uniform channel is obtained by including the perpendicular demagnetization and a finite-laser-distribution function (with a full width at half maximum of 700 nm). The upper inset is the schematics for the Oersted field angle, and the lower inset illustrates that the laser scans along the width of the channel (dotted line) for measuring θ_{Oe}.

the temporal profile of the thermal gradient. In contrast, the V_J pulse due to heating is determined by the temperature change. Finite-element simulation suggests that the absolute temperature (corresponding to V_J) has a slightly slower response to the laser pulse than the thermal gradient (corresponding to V_{ANE}) [19]. In addition, the temporal profile of the temperature has a slower delay as the heat diffuses into the substrate. As a result, the measured rf current phase in Fig. 3(b) has a forward phase shift compared to that measured with magnetic precession phase [Fig. 3(a)]. Finally, a separate fast-mixing experiment (using a narrower, approximately 80 ps reference pulse) also confirms a small but measurable delay ($\lesssim 20$ ps) between the absolute temperature and thermal gradient pulses.

Now we use the FMR phase relation established earlier in Eq. (4) to measure the spatial variation of the Oersted field. To do so, we use the sum of Eqs. (4a) and (4b) to obtain the effective Oersted field orientation:

$$\theta_{Oe} = (\varphi_{FMR}^{+} + \varphi_{FMR}^{-} + 180°)/2. \quad (5)$$

Note that the expression for θ_{Oe} is independent of φ_{rf}, and, hence, the measured θ_{Oe} is not affected by the random initial AWG phase φ_{AWG}^{0}. θ_{Oe} is measured as a function of the y position of the laser, as presented in Fig. 4. Though scattered, the data show a general trend that is consistent with the expected Oersted field distribution in the sample. Near the center of the structure, the Oersted field direction is mostly in plane: $\theta_{Oe} \approx 0$; while approaching either edge, the Oersted field tilts out of the plane, towards either the positive or negative z directions.

Next, we demonstrate the scanning capability with phase-sensitive imaging of both the FMR signal and rf current. We select two values of φ_{AWG} from the data in Figs. 2 and 3, 260° and 5° that, respectively, have a positive and negative resonance peak in the field-modulated signal. Figure 5 shows the imaging of the FMR signal (V_{mod}), rf current signal (V_{chop}), and reflectivity for the each AWG phase. Both the FMR signal and rf current signal change sign between the two phases, which is consistent with the previous results in Fig. 3. (Figures 3 and 5 have the same φ_{AWG}^{0}.) Regardless of its phase, we find that the rf current flows uniformly within the micrometer-scale bar structure, unlike the case of millimeter-scale channels where the rf current could be spatially varying [37], while the quasiuniform FMR signal appears to have a relatively broad distribution with a smooth variation near the edges.

So far, we have discussed the sample with a straight channel, in which case, the rf current is uniformly distributed and maintains constant phase inside the sample. In the following, we perform TRANE measurements on a nonuniform channel with a cross geometry. Although the cross displays a slightly more complicated scenario where both the amplitude and phase of the rf driving current is nonuniform, it better demonstrates TRANE's imaging capability for both the current and magnetic response. Figure 6(a) shows the magnetic imaging of the cross sample saturated in the y direction without the applied current. When measuring the cross structure, we connect the left and right contact pads to the rf current source, with the top and bottom pads left open. The measured V_{chop} remains sensitive to m_y under this configuration. Instead of a uniform magnetic signal shown in Fig. 1(d) for the bar

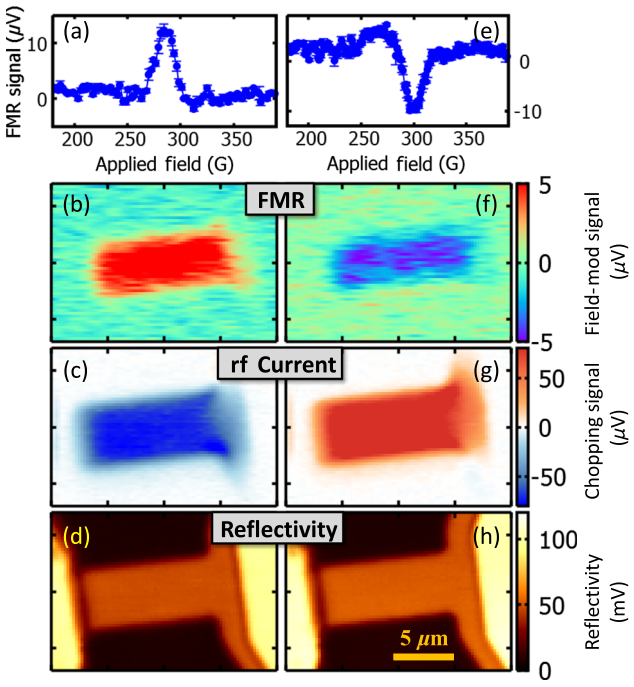

FIG. 5. Field-modulated FMR spectra with $\varphi_{\mathrm{AWG}} = 260°$ and 5°, respectively, showing either positive (a) or negative (e) signal at resonance. For the spectrum in (a), the applied field is fixed at 285 G where the peak locates while the FMR signal (b), rf current (c), and reflectivity (d) are measured simultaneously. (f)–(h) Similar imaging is recorded for the spectrum in (e) while the applied field is fixed at 300 G.

sample, the cross sample has a weaker signal at the center than that near the left and right pads. To explain the nonuniform magnetic signal, we note that V_{ANE} depends on geometric factors including channel width. In the regions where the focused laser diameter is less than the channel width, the locally generated current from E_{ANE} has closed paths that shunt some of the signal [19]. In this sample, especially in the cross junction, there are more current shunting paths available than there are near the left and right bond pads, which leads to a geometric reduction in signal strength that depends on position even though the magnetization is in a uniform, saturated state.

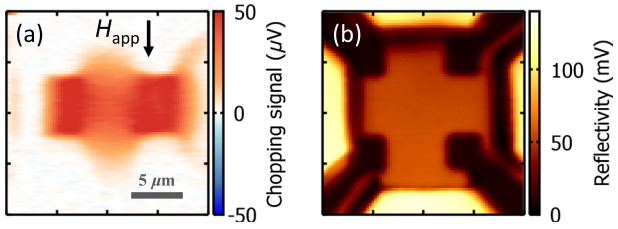

FIG. 6. (a) ANE imaging of the cross sample in the saturated state. A large magnetic field is applied along the y direction, with zero current applied. A pair of electrical contacts are connected to the left and right pads of the cross. (b) The reflectivity of the laser is measured along with the magnetic imaging.

We now apply the rf current to investigate the FMR imaging for the cross structure. Two different rf current phases are used, and for each current phase, both the FMR signal and the rf current are imaged. The results for $\varphi_{\mathrm{AWG}} = 310°$ are shown in Figs. 7(a)–(c), and the similar measurements are done for $\varphi_{\mathrm{AWG}} = 210°$ shown in Figs. 7(d)–(f). The most notable result is the imaging of Fig. 7(c) in which the current signal changes the sign across the sample. The rf current signal for $\varphi_{\mathrm{AWG}} = 210°$ does not change sign, although it does go through a phase shift. The FMR response shown in Figs. 7(b) and 7(e) also has a strong spatial variation, and it can even go through a sign change for particular AWG phases (not shown here). Last, by combining two current images [Figs. 7(c) and 7(f)] measured at different AWG phases, we can reconstruct the

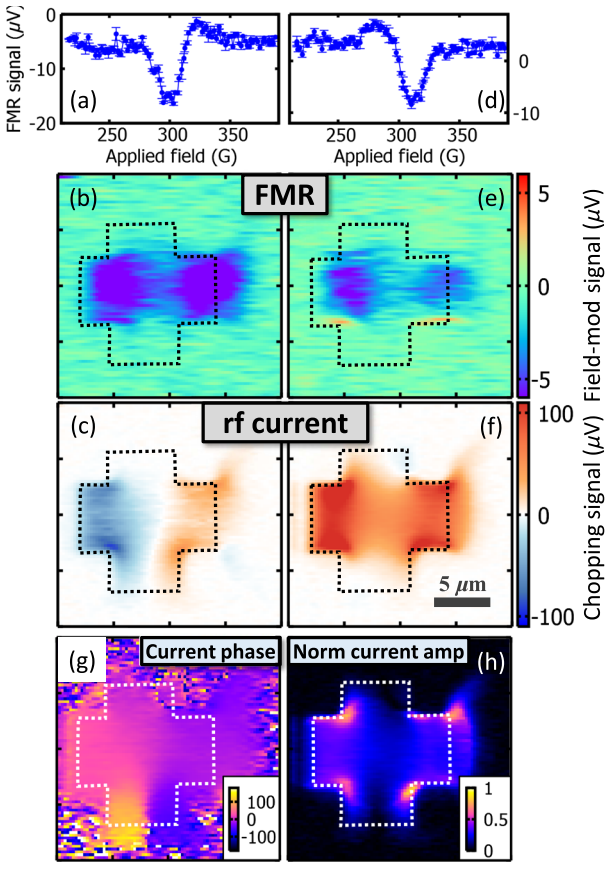

FIG. 7. (a) A FMR spectrum with $\varphi_{\mathrm{AWG}} = 310°$ measured at the right arm of the cross. (b),(c) show the FMR and rf current images, respectively, for the spectrum in (a) when the applied field is fixed at 300 G. (d) Another FMR spectrum $\varphi_{\mathrm{AWG}} = 210°$, also measured at the right arm of the cross, and its corresponding FMR (e) and rf current (f) imaging with the applied field fixed at 310 G. The images of relative current phase (g) and normalized current intensity (h) are reconstructed from (c),(f). The effect of the spatial dependence of the detection efficiency [Fig. 6(a)] is removed in the current intensity map. The dashed contours of the cross are obtained from the simultaneous reflectivity measurements.

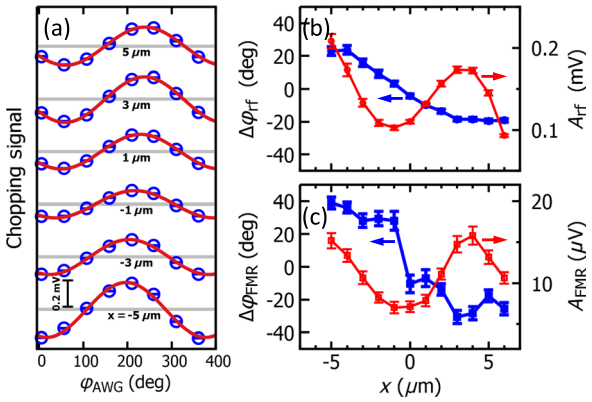

FIG. 8. (a) rf current signal as a function of AWG phase, measured at various x positions. $x = 0$ corresponds to the middle of the cross. The relative phase (solid blue) and amplitude (hollow red) for the rf current (b) and field-modulated FMR signal (c) are also measured as functions of x.

images for both the relative phase variation and the amplitude variation of the rf current shown in Figs. 7(g) and 7(h), respectively. We point out that the effect of the spatially nonuniform detection-efficiency function indicated in Fig. 6(a) is removed in the normalized current distribution in Fig. 7(h).

To further investigate the features imaged in the cross structure that are distinct from the bar structure, we measure the phase and the amplitude for both the rf current and FMR response at points along the x direction across the middle of the sample. The results are shown in Fig. 8. Note that the φ_{AWG} in Fig. 8 is consistent with that in Fig. 7, and the rf current sign change for $\varphi_{\mathrm{AWG}} = 310°$ is also observed in Fig. 8(a). As illustrated in Fig. 8(a), not only the amplitude but also the phase of the rf current varies with the x position. The current amplitude reduces at the cross center, which can be understood from current spreading and signal shunting previously observed in Fig. 6(a). However, the current phase varies monotonically across the sample plotted in Fig. 8(b). We attribute the phase shift of the current to the shape-dependent inductance. As the current follows along the sample, it encounters a geometry-induced inductance variation, particularly at the center, which alters the current phase. In company with the driving current, the FMR phase also decreases along x shown in Fig. 8(c). The amplitude of the FMR signal is also closely related to the rf current amplitude. We conclude that for these samples, where the sample dimension is much longer than the magnetic exchange length, the spatially dependent phase and amplitude of FMR precession is strongly influenced by the local excitation.

IV. CONCLUSION

In summary, we demonstrate simultaneous measurements of the local FMR and rf current using TRANE microscopy and its extensions. We study samples driven solely by Oersted fields to establish a quantitative phase relation between excitation current and magnetic response at gigahertz frequency, which is useful for future research of spin-torque devices. We also show stroboscopic imaging of both the stimulus and the magnetic response using simple uniform-width channels. With a nontrivial cross-channel geometry, the rf current and, thus, the FMR response are strongly nonuniform.

ACKNOWLEDGEMENTS

We thank Dr. Graham Rowlands, Dr. Praveen Gowtham, and Minh-Hai Nguyen for helpful discussions. This work is supported by AFOSR under Contract No. FA9550-14-1-0243. This work makes use of the Cornell Center for Materials Research Shared Facilities which are supported through the NSF MRSEC Program No. DMR-1120296, as well as the Cornell NanoScale Facility, a member of the National Nanotechnology Coordinated Infrastructure Network supported by the NSF Grant No. ECCS-15420819.

[1] Sergej O. Demokritov and Vladislav E. Demidov, Micro-Brillouin light scattering spectroscopy of magnetic nanostructures, IEEE Trans. Magn. **44**, 6 (2008).

[2] H. T. Nembach, Justin M. Shaw, T. J. Silva, W. L. Johnson, S. A. Kim, R. D. McMichael, and P. Kabos, Effects of shape distortions and imperfections on mode frequencies and collective linewidths in nanomagnets, Phys. Rev. B **83**, 094427 (2011).

[3] R. L. Stamps and R. E. Camley, *Solid State Physics* (Academic Press, San Diego, CA, 2012), Vol. 63.

[4] S. Urazhdin, V. E. Demidov, H. Ulrichs, T. Kendziorczyk, T. Kuhn, J. Leuthold, G. Wilde, and S. O. Demokritov, Nanomagnonic devices based on the spin-transfer torque, Nat. Nanotechnol. **9**, 509 (2014).

[5] O. Klein, G. de Loubens, V. V. Naletov, F. Boust, T. Guillet, H. Hurdequint, A. Leksikov, A. N. Slavin, V. S. Tiberkevich, and N. Vukadinovic, Ferromagnetic resonance force spectroscopy of individual submicron-size samples, Phys. Rev. B **78**, 144410 (2008).

[6] Inhee Lee, Yuri Obukhov, Gang Xiang, Adam Hauser, Fengyuan Yang, Palash Banerjee, Denis V. Pelekhov, and P. Chris Hammel, Nanoscale scanning probe ferromagnetic resonance imaging using localized modes, Nature (London) **466**, 845 (2010).

[7] Han-Jong Chia, Feng Guo, L. M. Belova, and R. D. McMichael, Nanoscale Spin Wave Localization Using Ferromagnetic Resonance Force Microscopy, Phys. Rev. Lett. **108**, 087206 (2012).

[8] Han-Jong Chia, Feng Guo, L. M. Belova, and R. D. McMichael, Spectroscopic defect imaging in magnetic nanostructure arrays, Appl. Phys. Lett. **101**, 042408 (2012).

[9] Feng Guo, L. M. Belova, and R. D. McMichael, Spectroscopy and Imaging of Edge Modes in Permalloy Nanodisks, Phys. Rev. Lett. **110**, 017601 (2013).

[10] Rohan Adur, Chunhui Du, Hailong Wang, Sergei A. Manuilov, Vidya P. Bhallamudi, Chi Zhang, Denis V.

Pelekhov, Fengyuan Yang, and P. C. Hammel, Damping of Confined Modes in a Ferromagnetic Thin Insulating Film: Angular Momentum Transfer across a Nanoscale Field-Defined Interface, Phys. Rev. Lett. **113**, 176601 (2014).

[11] A. Hamadeh, O. d'Allivy Kelly, C. Hahn, H. Meley, R. Bernard, A. H. Molpeceres, V. V. Naletov, M. Viret, A. Anane, V. Cros, S. O. Demokritov, J. L. Prieto, M. Muñoz, G. de Loubens, and O. Klein, Full Control of the Spin-Wave Damping in a Magnetic Insulator Using Spin-Orbit Torque, Phys. Rev. Lett. **113**, 197203 (2014).

[12] W. K. Hiebert, A. Stankiewicz, and M. R. Freeman, Direct Observation of Magnetic Relaxation in a Small Permalloy Disk by Time-Resolved Scanning Kerr Microscopy, Phys. Rev. Lett. **79**, 1134 (1997).

[13] J. P. Park, P. Eames, D. M. Engebretson, J. Berezovsky, and P. A. Crowell, Spatially Resolved Dynamics of Localized Spin-Wave Modes in Ferromagnetic Wires, Phys. Rev. Lett. **89**, 277201 (2002).

[14] B. Hillebrands and K. Ounadjela, *Spin Dynamics in Confined Magnetic Structures II* (Springer, New York, 2003), Chap. 3.

[15] P. S. Keatley, P. Gangmei, M. Dvornik, R. J. Hicken, J. R. Childress, and J. A. Katine, Large amplitude magnetization dynamics and the suppression of edge modes in a single nanomagnet, Appl. Phys. Lett. **98**, 082506 (2011).

[16] V. Chembrolu, J. P. Strachan, X. W. Yu, A. A. Tulapurkar, T. Tyliszczak, J. A. Katine, M. J. Carey, J. Stöhr, and Y. Acremann, Time-resolved x-ray imaging of magnetization dynamics in spin-transfer torque devices, Phys. Rev. B **80**, 024417 (2009).

[17] M. K. Marcham, P. S. Keatley, A. Neudert, R. J. Hicken, S. A. Cavill, L. R. Shelford, G. van der Laan, N. D. Telling, J. R. Childress, J. A. Katine, P. Shafer, and E. Arenholz, Phase-resolved x-ray ferromagnetic resonance measurements in fluorescence yield, J. Appl. Phys. **109**, 07D353 (2011).

[18] Andreas Vogel, Thomas Kamionka, Michael Martens, André Drews, Kang Wei Chou, Tolek Tyliszczak, Hermann Stoll, Bartel Van Waeyenberge, and Guido Meier, Coupled Vortex Oscillations in Spatially Separated Permalloy Squares, Phys. Rev. Lett. **106**, 137201 (2011).

[19] J. M. Bartell, D. H. Ngai, Z. Leng, and G. D. Fuchs, Table-top measurement of local magnetization dynamics using picosecond thermal gradients: Toward nanoscale magnetic imaging, Nat. Commun. **6**, 8460 (2015).

[20] A. A. Tulapurkar, Y. Suzuki, A. Fukushima, H. Kubota, H. Maehara, K. Tsunekawa, D. D. Djayaprawira, N. Watanabe, and S. Yuasa, Spin-torque diode effect in magnetic tunnel junctions, Nature (London) **438**, 339 (2005).

[21] J. C. Sankey, P. M. Braganca, A. G. F. Garcia, I. N. Krivorotov, R. A. Buhrman, and D. C. Ralph, Spin-Transfer-Driven Ferromagnetic Resonance of Individual Nanomagnets, Phys. Rev. Lett. **96**, 227601 (2006).

[22] Luqiao Liu, Takahiro Moriyama, D. C. Ralph, and R. A. Buhrman, Spin-Torque Ferromagnetic Resonance Induced by the Spin Hall Effect, Phys. Rev. Lett. **106**, 036601 (2011).

[23] Takahiro Moriyama, Seungha Yoon, and Robert D. McMichael, Ferromagnetic resonance measurement using stroboscopic magneto-optical Kerr effect, J. Appl. Phys. **117**, 213908 (2015).

[24] Abraham Slachter, Frank Lennart Bakker, and Bart Jan van Wees, Anomalous Nernst and anisotropic magnetoresistive heating in a lateral spin valve, Phys. Rev. B **84**, 020412 (2011).

[25] Mathias Weiler, Matthias Althammer, Franz D. Czeschka, Hans Huebl, Martin S. Wagner, Matthias Opel, Inga-Mareen Imort, Günter Reiss, Andy Thomas, Rudolf Gross, and Sebastian T. B. Goennenwein, Local Charge and Spin Currents in Magnetothermal Landscapes, Phys. Rev. Lett. **108**, 106602 (2012).

[26] Arndt von Bieren, Florian Brandl, Dirk Grundler, and Jean-Philippe Ansermet, Space- and time-resolved Seebeck and Nernst voltages in laser-heated permalloy/gold microstructures, Appl. Phys. Lett. **102**, 052408 (2013).

[27] Stephen M. Wu, Jason Hoffman, John E. Pearson, and Anand Bhattacharya, Unambiguous separation of the inverse spin Hall and anomalous Nernst effects within a ferromagnetic metal using the spin Seebeck effect, Appl. Phys. Lett. **105**, 092409 (2014).

[28] Kyeong-Dong Lee, Dong-Jun Kim, Hae Yeon Lee, Seung-Hyun Kim, Jong-Hyun Lee, Kyung-Min Lee, Jong-Ryul Jeong, Ki-Suk Lee, Hyon-Seok Song, Jeong-Woo Sohn, Sung-Chul Shin, and Byong-Guk Park, Thermoelectric signal enhancement by reconciling the spin Seebeck and anomalous Nernst effects in ferromagnet/non-magnet multilayers, Sci. Rep. **5**, 10249 (2015).

[29] The minus sign is merely due to the choice of the ground. We define the sign of the current to be consistent with that of the driving field h_{rf}, i.e., when $I_{\mathrm{rf}} > 0$, $h_{\mathrm{rf}} > 0$.

[30] K. Ando, S. Takahashi, K. Harii, K. Sasage, J. Ieda, S. Maekawa, and E. Saitoh, Electric Manipulation of Spin Relaxation Using the Spin Hall Effect, Phys. Rev. Lett. **101**, 036601 (2008).

[31] L. Liu, R. A. Buhrman, and D. C. Ralph, Review and analysis of measurements of the spin Hall effect in platinum, arXiv:1111.3702.

[32] A. Azevedo, L. H. Vilela-Leão, R. L. Rodríguez-Suárez, A. F. Lacerda Santos, and S. M. Rezende, Spin pumping and anisotropic magnetoresistance voltages in magnetic bilayers: Theory and experiment, Phys. Rev. B **83**, 144402 (2011).

[33] Weifeng Zhang, Wei Han, Xin Jiang, See-Hun Yang, and Stuart S. P. Parkin, Role of transparency of platinum-ferromagnet interfaces in determining the intrinsic magnitude of the spin Hall effect, Nat. Phys. **11**, 496 (2015).

[34] To obtain the precession angle θ_p, we use $\sin\theta_p/\sin 5° = 2V_{\mathrm{FMR}}/\Delta V_{\mathrm{chop}}$, where 5° is the titling angle of the in-plane applied field with respect to the x direction, V_{FMR} is the voltage amplitude of the FMR signal, and ΔV_{chop} is the voltage difference between opposite large fields in the hysteresis loop [Fig. 1(f)].

[35] Note that Eq. (2) is valid under small-modulation-field approximation. In our setup, we use a modulation field of about 7 G, and the full width at half maximum of the linewidth is typically around 33 G. Thus, the expression in Eq. (2) is adequate for fitting the spectra.

[36] The value of the AWG phase at the intersection suggests $\varphi^0_{\mathrm{AWG}} = \varphi^{\mathrm{intersec}}_{\mathrm{AWG}} = (137.9 \pm 4.0)°$.

[37] Vincent Vlaminck, Helmut Schultheiss, John E. Pearson, Frank Y. Fradin, Sam D. Bader, and Axel Hoffmann, Mapping microwave field distributions via the spin Hall effect, Appl. Phys. Lett. **101**, 252406 (2012).